# ON THE PREDICTION OF FLOW PATTERNS AND LOSSES IN HP AXIAL TURBINE STAGES USING 3D RANS SOLVER WITH TWO TURBULENCE MODELS

PIOTR LAMPART, JERZY ŚWIRYDCZUK
AND ANDRZEJ GARDZILEWICZ

*Institute of Fluid Flow Machinery*
*Polish Academy of Sciences,*
*Fiszera 14, 80-952 Gdansk, Poland*
*lampart@imp.gda.pl*

**Abstract:** An experimentally tested air turbine stage and a real high-pressure (HP) steam turbine stage are calculated using the 3D RANS solver FlowER supplemented with the Baldwin-Lomax and Menter shear stress transport (SST) models. The computations of the model air turbine stage show that the Menter SST model gives better agreement with the experimental data as far as the span-wise distribution of exit velocities and swirl angle. The comparison of performance of the two turbulence models exhibits differences in predicting flow patterns and losses in the considered HP turbine stage. The main differences concern the development of secondary flows and separations. There is a significant span-wise redistribution of losses between these two models. The tendency is that for the same relatively refined grid resolutions, the level of pitch/span averaged losses for the Menter SST turbulence model is slightly above that of Baldwin-Lomax.

**Keywords:** HP axial turbine, RANS equations, turbulence modelling, kinetic energy losses

## *Nomenclature*

In this chapter, main turbine characteristics often referred to in the paper, like stage reaction and kinetic energy losses in the stator, rotor and stage, are defined. The definitions are gathered in Table 1 and are easily explained with the help of Figure 1, which illustrates the process of expansion in a turbine stage in the form of an enthalpy-entropy diagram.

**Table 1.** Reaction, kinetic energy losses in the stator, rotor and stage

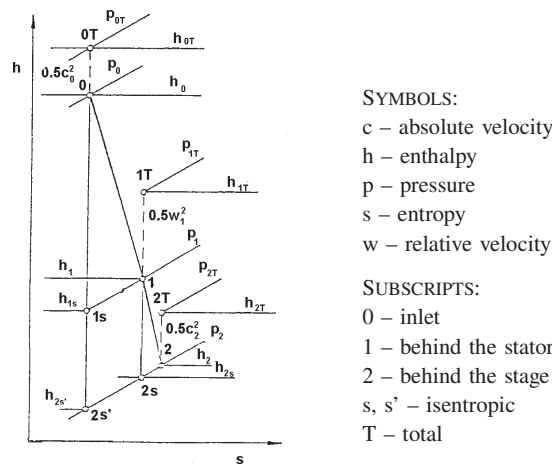| | |
|---|---|
| Reaction | $\rho = (h_1 - h_{2s})/(h_{0T} - h_{2s})$ |
| Stator loss | $\xi_1 = (h_1 - h_{1s})/(h_{0T} - h_{1s})$ |
| Rotor loss | $\xi_2 = (h_2 - h_{2s})/(h_{1T} - h_{2s})$ |
| Stage loss (without exit energy) = stator + rotor loss | $\xi_{12} = (h_2 - h_{2s})/(h_{0T} - h_{2s})$ |
| Stage loss (with exit energy) | $\xi_{12c} = (h_{2T} - h_{2s})/(h_{0T} - h_{2s})$ |

**Figure 1.** Enthalpy-entropy diagram for a turbine stage

## 1. **Introduction**

Simulation of turbulent effects is of great importance for the computation of 3D viscous compressible turbomachinery flows. There are a number of turbulence models ranging from algebraic eddy-viscosity to differential Reynolds stress models. None of them has been reported so far to correctly describe all types of flows. Therefore, it is crucial that a chosen model should be appropriate for the investigated flow and easy to implement without considerably increasing computational costs. The simplest turbulence model is an algebraic two-layer eddy-viscosity model of Baldwin-Lomax [1] that has become a standard for turbomachinery codes. Its great assets are easy numerical implementation, relative numerical stability, reasonable performance in wall regions, and low CPU costs. A disadvantage is that the model performs poorer in adverse pressure gradient boundary layers and free shear flows away from body surfaces, and does not account for effects of inlet free-stream turbulence.

Two-equation models are also very often developed as closures of RANS solvers. There are a variety of $k$-$\varepsilon$ models, including those of Jones and Launder [2], Launder and Sharma [3] or Chien [4]. The $k$-$\varepsilon$ models are known to perform relatively well in free shear layer flows. On the other hand, they require a number of damping functions near the walls, and even with damping functions they are unable to predict well velocity profiles and skin friction in high-Reynolds number flows.

Unlike $k$-$\varepsilon$ models, a series of $k$-$\omega$ models, see Wilcox [5], Chima [6], do not need damping functions near the wall and allow a simple Dirichlet condition to be specified there. Truly inconsistent here, an asymptotic behaviour of $\omega$ as it approaches the wall is usually replaced by a finite value, as the molecular viscosity in the boundary layer exceeds the eddy-viscosity and the form of turbulence here does not necessarily have an effect on the mean velocity profiles and skin friction. The $k$-$\omega$ model of Wilcox is also capable of treating rough walls and surface mass injections, and is also superior to the $k$-$\varepsilon$ in compressible flows. Another model of Wilcox [7] contains extra functions to improve the transition. One drawback of the $k$-$\omega$ models is their excessive sensitivity to the free-stream value of $\omega$, a deficiency not featuring in the $k$-$\varepsilon$ approach.

An idea put forward by Menter [8] is to combine good features of both $k$-$\omega$ and $k$-$\varepsilon$ models, at the same time eliminating their deficiencies. This is pronounced in his new model called the baseline model (BSL) where $k$-$\omega$ model is activated in the near wall region, and then switched to the $k$-$\varepsilon$ model in the wake region and free shear layers. The formulation of the standard high-Reynolds number $k$-$\varepsilon$ model is transformed to a $k$-$\omega$ formulation. It is then multiplied by sides by a blending function $(1 - F_1)$ and added to an original formulation of the $k$-$\omega$ model multiplied by $F_1$, with the blending function $F_1$ changing from 1 in the logarithmic region of the boundary layer gradually to 0 in the wake region.

Departing from this model, Menter [8] also proposed another model he refers to as the shear stress transport model (SST), modifying the eddy viscosity so as to account for the effects of turbulent shear stress transport. The idea is based on Bradshaw's experimental observations that the principal turbulent shear stress is proportional to the turbulent kinetic energy in the wake region of the boundary layer. Arguing that superior performance of the $k$-$\omega$ model in the logarithmic region of the boundary layer has a limited effect on the eddy viscosity in the wake region which finally determines the ability of an eddy-viscosity model to predict strong adverse pressure gradient flows, and referring to the results of the model of Johnson and King [9] that enforces the Bradshaw's observation and shows an improvement over standard algebraic models by reducing the wake region eddy viscosity in adverse pressure gradient flows, Menter redefines the eddy viscosity into a form $\nu_t = a_1 k / \max(a_1 \omega, \Omega F_2)$, where $a_1$ is the Bradshaw constant, $\Omega$ – vorticity (absolute value) and $F_2$ is a function that changes from 1 in boundary layer flows to 0 for free shear layers. Due to the fact that in adverse pressure gradient boundary layers the production of turbulent kinetic energy is larger than its dissipation, the above formulation guarantees the proportional relationship between the principal turbulent shear stress and the turbulent kinetic energy in the boundary layer ($\tau = \nu_t \Omega = \rho a_1 k$).

Differential or algebraic Reynolds stress models form a great potential to improve predictions from RANS solvers. However, numerical implementation or numerical stability is still an unresolved question here, also in classical test cases, not only with respect to complex turbomachinery geometries. Therefore, software developers still tend to hold on to simple but robust algebraic or two-equation eddy-viscosity models and improve them for particular applications. This tendency is also preserved in development of a code FlowER – RANS solver of 3D viscous compressible flows in axial and radial turbomachinery shortly described below, see also Yershov and Rusanov [10, 11], Yershov *et al.* [12]. A comprehensive review of turbulence modelling for CFD codes can be found for example in a book of Wilcox [13], paper of Menter [14] and dissertation of Larsson [15].

The paper of Yershov *et al.* [16] indicates that the Menter SST model has an upper hand over the Baldwin-Lomax model in modelling transonic compressor flows, for example ROTOR 37. For this case, it turned out to be impossible to compute over the entire range of operation of the compressor using the Baldwin-Lomax model, whereas the Menter SST model yielded a very good agreement between the experimental and computational results, including the total pressure ratio and adiabatic efficiency over the entire operational range of the compressor. The aim of the present paper is to test the performance of the two-equation eddy-viscosity shear stress transport model of Menter as superior between the two-equation models, compared to the performance of the modified algebraic eddy-viscosity model of

Baldwin-Lomax, in the context of predicting flow patterns and efficiency characteristics for HP model and real turbine stages.

## 2. 3D RANS solver

### 2.1. Basic equations

3D flow of viscous and compressible gas through a turbine stage can be described by a set of unsteady Reynolds-averaged Navier-Stokes equations written in a curvilinear body-fitted coordinate system $(\xi, \eta, \zeta)$, rotating with an angular speed $\varpi$ (the computational domain extends on blade-to-blade passages, axial gaps and radial gaps above/below unshrouded blade tips)

$$\frac{\partial QJ}{\partial t} + \frac{\partial \left(E\xi_x + F\xi_y + G\xi_z\right)J}{\partial \xi} + \frac{\partial \left(E\eta_x + F\eta_y + G\eta_z\right)J}{\partial \eta} + \frac{\partial \left(E\zeta_x + F\zeta_y + G\zeta_z\right)J}{\partial \zeta} = HJ, \quad (1)$$

where: $Q = \begin{bmatrix} \rho \\ \rho u \\ \rho v \\ \rho w \\ h \end{bmatrix}$; $H = \begin{bmatrix} 0 \\ 2\rho v\varpi + \rho\varpi^2 r_x \\ -2\rho u\varpi + \rho\varpi^2 r_y \\ 0 \\ 0 \end{bmatrix}$; $E = \begin{bmatrix} \rho u \\ \rho u^2 + p - \tau_{xx} \\ \rho uv - \tau_{xy} \\ \rho uw - \tau_{xz} \\ (h+p)u - u\tau_{xx} - v\tau_{xy} - w\tau_{xz} + q_x \end{bmatrix}$;

$$F = \begin{bmatrix} \rho v \\ \rho uv - \tau_{xy} \\ \rho v^2 + p - \tau_{yy} \\ \rho vw - \tau_{yz} \\ (h+p)v - u\tau_{xy} - v\tau_{yy} - w\tau_{yz} + q_y \end{bmatrix}; \quad G = \begin{bmatrix} \rho w \\ \rho uw - \tau_{xz} \\ \rho vw - \tau_{yz} \\ \rho w^2 + p - \tau_{zz} \\ (h+p)w - u\tau_{xz} - v\tau_{yz} - w\tau_{zz} + q_z \end{bmatrix};$$

$$h = \frac{1}{\gamma - 1}\frac{p}{\rho} + \frac{u^2 + v^2 + w^2 - \varpi^2 r^2}{2} + const; \quad q = -\lambda \nabla T;$$

$$\tau_{ij} = \tau_{m_{ij}} + \tau_{t_{ij}}; \quad \tau_{m_{ij}} = 2\mu_m \left(S_{ij} - S_{nn}\delta_{ij}/3\right); \quad \tau_{t_{ij}} = 2\mu_t \left(S_{ij} - S_{nn}\delta_{ij}/3\right) - 2\rho k\delta_{ij}/3.$$

The symbols $p$, $\rho$, $u$, $v$, $w$ represent the pressure, density and components of the velocity, while $\tau_{m_{ij}}$, $\tau_{t_{ij}}$, $\tau_{ij}$ are molecular, turbulent and total viscous stress, $S_{ij}$ – mean strain-rate tensor; $T$ – temperature; $\mu = (\mu_m + \mu_t)$ – effective (molecular + turbulent) viscosity, $q$ – heat flux, $\lambda = \lambda_m + \lambda_t = c_p(\mu_m/Pr_m + \mu_t/Pr_t)$ – effective (molecular + turbulent) heat conductivity, $Pr_m$, $Pr_t$ – molecular and turbulent Prandtl numbers. The turbulence effects are modelled using two eddy-viscosity models – an algebraic model of Baldwin-Lomax and two-equation model of shear stress transport (SST) proposed by Menter.

### 2.2. Baldwin-Lomax turbulence model

In the original Baldwin-Lomax model the boundary layer is divided into two domains – an inner and outer layer. The turbulent viscosity in the inner region is calculated from the Prandtl concept of mixing length

$$\mu_{turb} = \mu^i_{turb} = \rho l^2 \Omega, \quad (2)$$

where $\Omega$ is the vorticity (absolute value), $l$ – mixing length

$$l = ky\left[1 - \exp\left(-y^+/A^+\right)\right]; \quad y^+ = y\sqrt{\rho_w/\tau_w}/\mu_w,$$

where $y$ is a distance from the wall, $\tau_w$ – wall shear stress, k = 0.41 (Kármán constant), $A^+ = 26$ (van Driest constant).

The turbulent viscosity in the outer region of the boundary layer is defined by the modified Clauser formula

$$\mu_{turb} = \mu_{turb}^0 = \alpha \, C_{CP} \, \rho \, F_{WK} \, F_k \,, \tag{3}$$

where $\alpha = K_{CL} \frac{1.55}{1+\varphi}$, $K_{CL} = 0.0168$ (Clauser constant), $C_{CP} = 1.6$, $\varphi = 0.55 \left[ 1 - \exp \left( -0.243 \sqrt{z} - 0.298 z \right) \right]$, $z = Re_\theta / 425 - 1$, $Re_\theta = \frac{\rho U \theta}{\mu}$.

$F_{WK}$ is the wake function

$$F_{WK} = \min \left( \eta_{\max} F_{\max}, C_{WK} y_{\max} U_D^2 / F_{\max} \right) \,,$$

where $U_D = U_{\max} - U_{\min}$ is a difference between the maximum and minimum velocity at the boundary layer section; $C_{WK} = 0.25$ (wake constant); $F_{\max}$ and $y_{\max}$ are found from the maximum of the function

$$F(y) = y \Omega \left[ 1 - \exp \left( y^+ / A^+ \right) \right] \,.$$

$F_k$ is the Klebanoff intermittency factor

$$F_k = \left[ 1 + 5.5 \left( C_k y / y_{\max} \right)^6 \right]^{-1} \,,$$

where $C_k = 0.3$ (Klebanoff constant). The division between the inner and outer layer is set at a point nearest to the wall where

$$\mu_{turb}^i = \mu_{turb}^0 \,.$$

The flow is assumed turbulent if at some point of the boundary layer profile the eddy viscosity calculated as prescribed above is 14 time larger than the molecular viscosity of undisturbed flow. Otherwise, the boundary layer is thought to be laminar at this section. The original model of Baldwin-Lomax was modified to improve its calculation of eddy viscosity in the regions of separation and wake. The modifications used in the code FlowER are described in Yershov and Rusanov [17], and also in the previous publication of the authors in the *TASK Quarterly* – see Yershov *et al.* [12]. The reader can also find there how to implement an originally 2D model in three dimensions with the description of a procedure accounting for intersecting effects of different walls and regions (endwalls and blade walls; wake, tip leakage). The resultant turbulent viscosity is obtained there as an average of turbulent viscosities calculated with respect to different walls (regions) for independent length scales, weighted with the distance to the other wall (region).

## 2.3. Menter's models of turbulence

The essence of Menter's idea is to use the $k$-$\varepsilon$ and $k$-$\omega$ turbulence models in the areas, where each of them better fits the reality. To do so, first the $k$-$\varepsilon$ model is transformed to the $k$-$\omega$ form and then the two models are combined using a blending function $F_1$ which switches between the models in the areas of their applicability.

The original $k$-$\omega$ model has the form

$$\begin{aligned}
\frac{\partial(\rho k)}{\partial t} + \frac{\partial(\rho k u_i)}{\partial x_i} &= \tau_{ij} \frac{\partial u_i}{\partial x_j} - \beta^* \rho \omega k + \frac{\partial}{\partial x_j} \left[ (\mu + \sigma_{k1} \mu_t) \frac{\partial k}{\partial x_j} \right] , \\
\frac{\partial(\rho \omega)}{\partial t} + \frac{\partial(\rho \omega u_i)}{\partial x_i} &= \frac{\gamma_1 \omega}{k} \tau_{ij} \frac{\partial u_i}{\partial x_j} - \beta_1 \rho \omega^2 + \frac{\partial}{\partial x_j} \left[ (\mu + \sigma_{\omega1} \mu_t) \frac{\partial \omega}{\partial x_j} \right] ,
\end{aligned} \tag{4}$$

where $k$ is the turbulent kinetic energy, $\omega$ – specific dissipation rate, $u_i$ – velocity component, $x_i$ – spatial coordinate.

The original $k$-$\varepsilon$ model can be written as

$$\frac{\partial(\rho k)}{\partial t} + \frac{\partial(\rho k u_i)}{\partial x_i} = \tau_{ij}\frac{\partial u_i}{\partial x_j} - \rho\varepsilon + \frac{\partial}{\partial x_j}\left[\left(\mu + \frac{\mu_t}{\sigma_k}\right)\frac{\partial k}{\partial x_j}\right],$$

$$\frac{\partial(\rho\varepsilon)}{\partial t} + \frac{\partial(\rho\varepsilon u_i)}{\partial x_i} = C_{\varepsilon 1}\frac{\varepsilon}{k}\tau_{ij}\frac{\partial u_i}{\partial x_j} - C_{\varepsilon 2}\frac{\rho\varepsilon^2}{k} + \frac{\partial}{\partial x_j}\left[\left(\mu + \frac{\mu_t}{\sigma_\varepsilon}\right)\frac{\partial\varepsilon}{\partial x_j}\right].$$

(5)

With the use of $\omega = \dfrac{\varepsilon}{k\beta^*}$, the set of Equations (5) can be transformed, after some algebra, to the $k$-$\omega$ form

$$\frac{\partial(\rho k)}{\partial t} + \frac{\partial(\rho k u_i)}{\partial x_i} = \tau_{ij}\frac{\partial u_i}{\partial x_j} - \beta^*\rho\omega k + \frac{\partial}{\partial x_j}\left[(\mu + \sigma_{k2}\mu_t)\frac{\partial k}{\partial x_j}\right],$$

$$\frac{\partial(\rho\omega)}{\partial t} + \frac{\partial(\rho\omega u_i)}{\partial x_i} = \frac{\gamma_2\omega}{k}\tau_{ij}\frac{\partial u_i}{\partial x_j} - \beta_2\rho\omega^2 + \frac{\partial}{\partial x_j}\left[(\mu + \sigma_{\omega 2}\mu_t)\frac{\partial\omega}{\partial x_j}\right] + \frac{2\rho\sigma_{\omega 2}}{\omega}\frac{\partial k}{\partial x_j}\frac{\partial\omega}{\partial x_j}.$$

(6)

The relations between the constants in the original and transformed forms of the $k$-$\varepsilon$ model are

$$\gamma_2 = C_{\varepsilon 1} - 1; \quad \beta_2 = \beta^*(C_{\varepsilon 2} - 1); \quad \sigma_{k2} = \frac{1}{\sigma_k}; \quad \sigma_{\omega 2} = \frac{1}{\sigma_\varepsilon}.$$

Now, the set of Equations (4) for the $k$-$\omega$ model is multiplied by $F_1$, and the set of Equations (6), representing the $k$-$\varepsilon$ model, by $(1 - F_1)$. After superposition, the two sets of equations take the following vector form giving the model referred to by Menter as the baseline model

$$\frac{\partial U}{\partial t} + \frac{\partial R_i}{\partial x_i} = G - D + L,$$

(7)

where: $U = \begin{bmatrix} \rho k \\ \rho\omega \end{bmatrix}$; $\quad R_i = \begin{bmatrix} \rho k - (\mu + \sigma_k\mu_t)\dfrac{\partial k}{\partial x_i} \\ \rho\omega - (\mu + \sigma_\omega\mu_t)\dfrac{\partial\omega}{\partial x_i} \end{bmatrix}$; $\quad G = \begin{bmatrix} \tau_{ij}S_{ij} \\ \gamma\dfrac{\omega}{k}\tau_{ij}S_{ij} \end{bmatrix}$; $\quad D = \begin{bmatrix} \beta^*\rho\omega k \\ \beta\rho\omega^2 \end{bmatrix}$;

$$L = \begin{bmatrix} 0 \\ 2(1 - F_1)\dfrac{\rho\sigma_{\omega 2}}{\omega}\dfrac{\partial k}{\partial x_i}\dfrac{\partial\omega}{\partial x_i} \end{bmatrix}.$$

The blending function $F_1$ which assures smooth transition from the $k$-$\omega$ model at the wall to the $k$-$\varepsilon$ model in free shear layers has the form

$$F_1 = \tanh\left\{[\min(A_1; A_2)]^4\right\},$$

where: $A_1 = \max(B_1; B_2); \quad A_2 = \dfrac{4\rho\sigma_{\omega 2}k}{CD_{k\omega}y^2}; \quad B_1 = \dfrac{\sqrt{k}}{\beta^*\omega y}; \quad B_2 = \dfrac{500\mu}{\rho y^2\omega};$

$$CD_{k\omega} = \max\left(2\frac{\rho\sigma_{\omega 2}}{\omega}\frac{\partial k}{\partial x_i}\frac{\partial\omega}{\partial x_i}; 10^{-20}\right).$$

A vector of constants $\phi = [\sigma_k, \sigma_\omega, \beta, \gamma]$ can be written as $\phi = F_1\phi_1 + (1 - F_1)\phi_2$, where $\phi_1$ is this vector in the $k$-$\omega$ model, and $\phi_2$ in the $k$-$\varepsilon$ model written in $k$-$\omega$ formulation. The constants of the baseline model assume values:

$$\sigma_{k1} = 0.5; \quad \sigma_{k2} = 1.0; \quad \sigma_{\omega 1} = 0.5; \quad \sigma_{\omega 2} = 0.856;$$

$$\beta^* = 0.09; \quad \beta_1 = 0.075; \quad \beta_2 = 0.0828; \quad \gamma_1 = 0.553; \quad \gamma_2 = 0.44.$$

Due to the fact that two-equation models fail in strong adverse pressure gradient flows, Menter introduced another model called the SST model where he redefined the eddy

viscosity so as to preserve the proportional relationship between the principal turbulent shear stress and turbulent kinetic energy in the boundary layer

$$\mu_t = \frac{\rho k/\omega}{\max[1; \Omega F_2/(a_1\omega)]}.$$

The blending function $F_2$ changes from 1 in boundary layer flows to 0 for free shear layers and has the form

$$F_2 = \tanh\left\{[\max(2B_1; B_2)]^2\right\}$$

with functions $B_1$, $B_2$ defined as before. The constants of the shear stress transport model are the same as for the baseline model save for $a_1 = 0.31$ (Bradshaw constant), $\sigma_{k1} = 0.85$.

### 2.4. Boundary conditions

The following boundary conditions are incorporated for the set of Equations (1):

– at the walls – no-slip and no heat flux;
– at the inlet – span-wise distribution of the total pressure, total temperature and flow angles at the inlet to the stage;
– at the exit – static pressure (either its span-wise distribution or a value at the mid-span with the radial equilibrium equation).

For the set of Equations (7), the boundary conditions are:
– at the walls:

$$k = 0, \quad \omega = \frac{60\mu_w}{\rho_w \beta y^2};$$

– at the inlet:

$$k = \frac{3}{2}(Tu \cdot U_\infty)^2, \quad \omega = \sqrt{\frac{\max(S\Omega, \Omega^2)}{\beta^*}}, \quad S = \sqrt{\frac{1}{2}S_{ij}S_{ij}},$$

where $Tu$ – inlet free-stream turbulence level.
– at the outlet: values of $k$ and $\omega$ are extrapolated from the preceding cell centres.

The computations are carried out in one blade-to-blade passage of the stator and rotor, and converge to a steady state with the condition of spatial periodicity and mixing plane approach assumed. The implemented inlet/exit boundary conditions impose the pressure drop and let the mass flow rate be resultant. The comparative calculations are performed for the same pressure drop across the stage.

### 2.5. Numerical scheme

The governing equations are solved numerically based on cell-centred finite-volume discretisation, Godunov-type upwind differencing, high resolution ENO scheme, and implicit operator $\delta$ of Beam and Warming, see Yershov *et al.* [12].

## 3. Model air turbine stage – comparison of experimental and computational results

The considered model air turbine stage of the Institute of Thermal Engineering (ITC) Łódź – model TK9-TW3, see Wiechowski [18], has a geometry typical for HP turbine stages. It operates with short-height cylindrical blading and aft-loaded stator profiles of aspect ratios: span/chord – 0.73 (stator) and 2.20 (rotor), pitch/chord – 0.86 (stator) and 0.80 (rotor), span/diameter – 0.08 (stator and rotor). The thermodynamic conditions are:
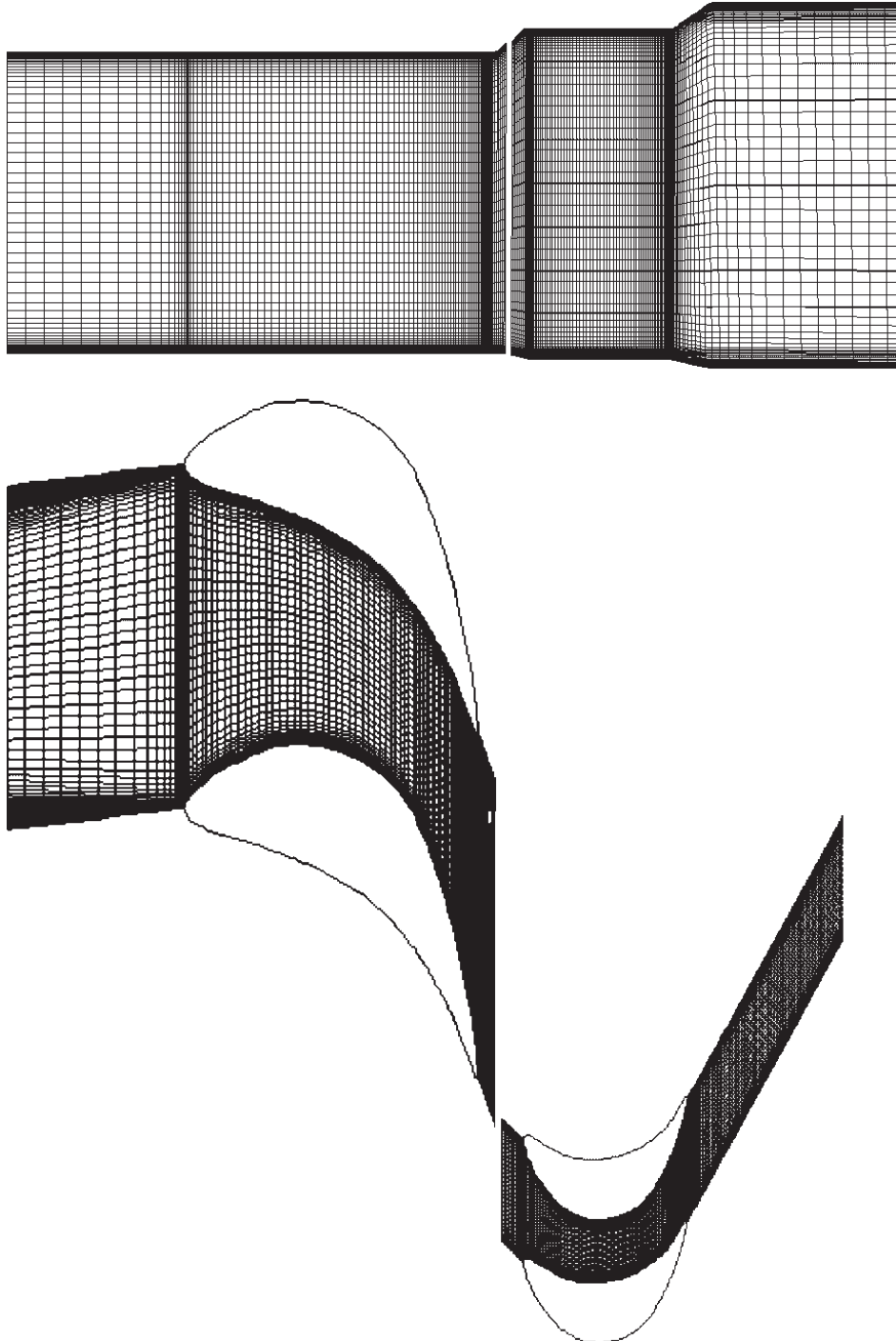
**Figure 2.** Computational grid for the stator and rotor cascades of the model turbine stage in meridional view (top) and in the blade-to-blade section at the mid-span (bottom)
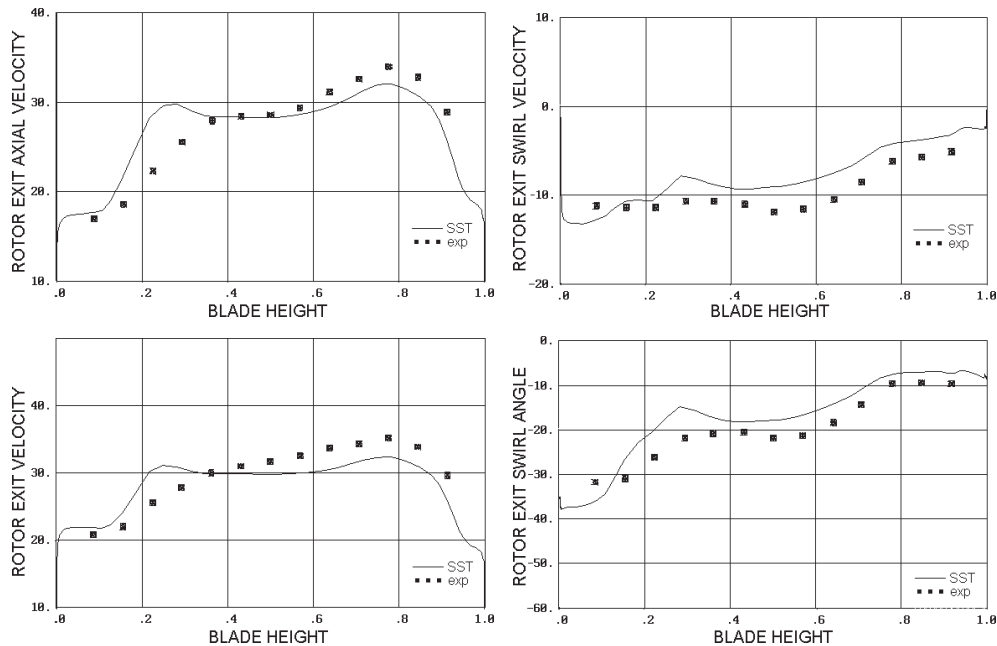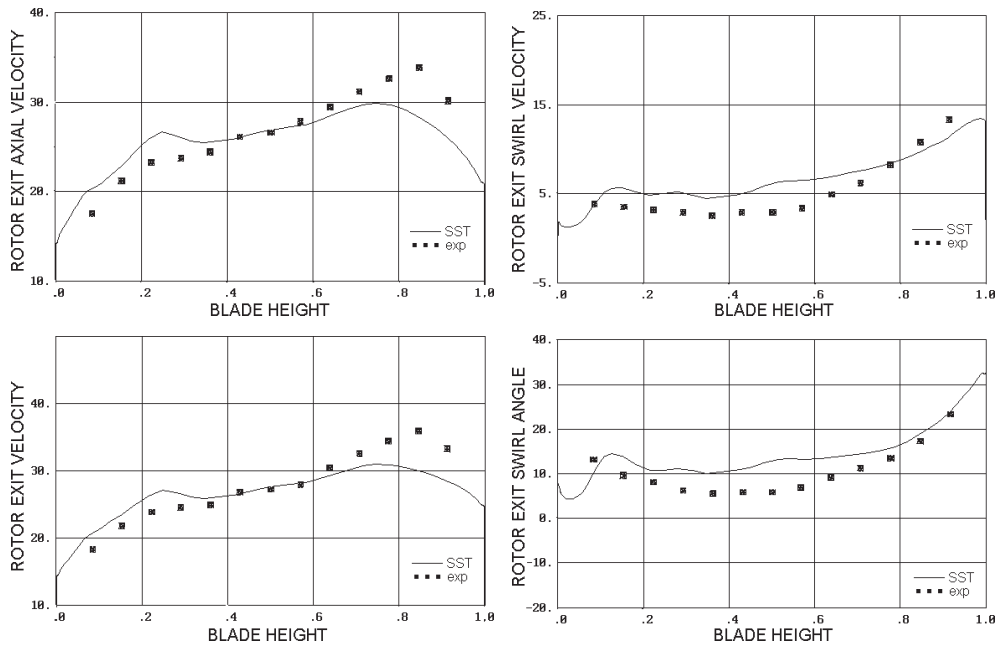
**Figure 3.** The comparison of computed (SST) and experimental axial velocity (top left), absolute swirl velocity (top right), absolute velocity (bottom left) and absolute swirl angle (bottom right) at the exit from the rotor for $u/c_{0T} = 0.45$

the pressure drop from 1 to 0.9 bar, inlet temperature – 320 K, average reaction – 0.23 (nominal conditions), mass flow rate – 4.0 kg/s (nominal conditions). The turbine stage was investigated experimentally in [18] over a wide range of operating conditions $u/c_{0T}$ between 0.3 and 0.9 ($u$ – rotor speed at the mid-span, $c_{0T}$ – theoretical enthalpy drop across the stage), achieved by changing the rotor rotational speed. The available experimental data do not show field contours but disclose stage efficiencies, reactions at the hub and tip, as well as span-wise distributions of exit velocities (including axial and circumferential components) and swirl angle for the stator and rotor in the tested range of operating conditions. Therefore, these quantities will also be sought for in the process of computations of the model TK9-TW3 to validate the considered models of turbulence.

The computations were carried out for three values of $u/c_{0T}$ equal to 0.45, 0.54 (nominal conditions) and 0.65. The specific heat ratio and gas constant for the air were assumed as $\gamma = 1.401$ and $R = 283$ J/(kg K). An H-type grid of 1 200 000 cells (stator and rotor) refined near the endwalls, blade walls, trailing and leading edges was assumed for the computations. Gridding of the flow domain in the meridional view and in the blade-to-blade section at the mid-span is presented in Figure 2. The total pressure profile at the inlet is assumed uniform, with the inlet endwall boundary layers of thickness 2% of the blade span each, and low inlet free-stream turbulence level.

Figures 3–5 show the comparison of computational results, obtained with the help of the Menter SST model of turbulence, with experimental data for the axial velocity, absolute swirl velocity, absolute velocity and absolute swirl angle (measured from the direction normal to the cascade front) at the exit from the rotor for $u/c_{0T} = 0.45$, 0.54 and 0.65. The computed distributions were captured at the section located 135% of the

**Figure 4.** The comparison of computed (SST) and experimental axial velocity (top left), absolute swirl velocity (top right), absolute velocity (bottom left) and absolute swirl angle (bottom right) at the exit from the rotor for $u/c_{0T} = 0.54$
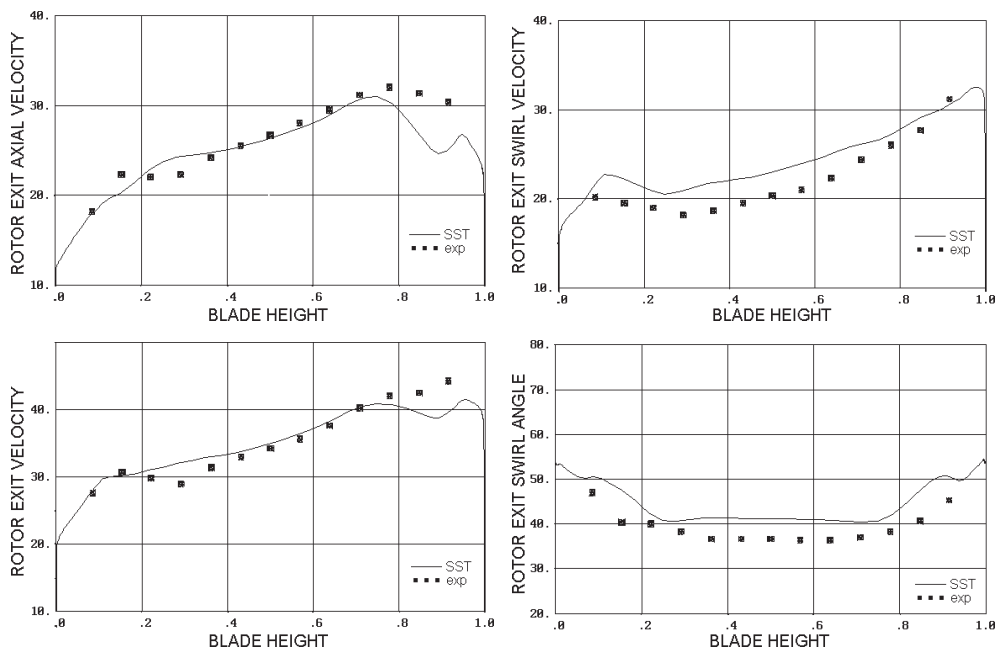


**Figure 5.** The comparison of computed (SST) and experimental axial velocity (top left), absolute swirl velocity (top right), absolute velocity (bottom left) and absolute swirl angle (bottom right) at the exit from the rotor for $u/c_{0T} = 0.65$
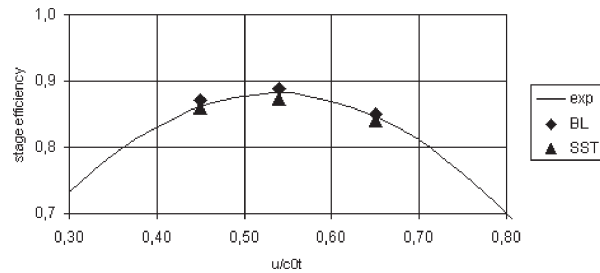
**Figure 6.** Computed and experimental efficiency characteristics of the model air turbine stage as a function of load $u/c_{0T}$
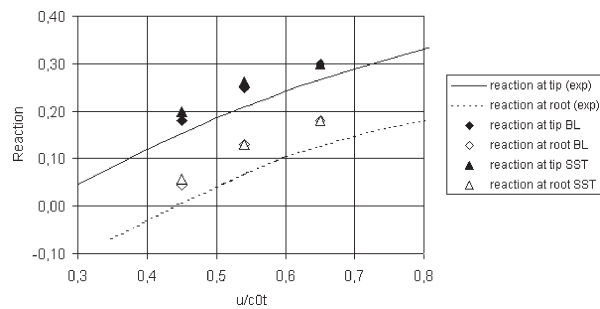


**Figure 7.** Computed and experimental reaction of the model air turbine stage at the tip and root as a function of load $u/c_{0T}$

axial chord downstream of the rotor trailing edge, that is at a distance corresponding to the location of the measuring probe at the experimental facility. In general, the computational and experimental results for all compared quantities reveal satisfactory qualitative and also quantitative agreement for the three investigated values of load. The reference section is relatively far downstream of the blading system, therefore, it is expected that the processes of mixing and dissipation of 3D flow structures are largely accomplished there. This is way the distributions of the investigated quantities do not exhibit considerable 3D peaks characteristic for sections more upstream. Nevertheless, the span-wise locations of those largely dissipated peaks as well as other non-uniformities of distributions are reproduced well. The results obtained for this paper with the help of the Menter SST closure seem to agree better with the experimental results than those presented in the previous work of the authors (jointly with authors of the code FlowER), published in *TASK Quarterly* [12], concerning the simulation of turbomachinery flows with the help of the code FlowER and the Baldwin-Lomax turbulence model. The comparison of computed and experimental results in [12], which will not be repeated here, was made for the model turbine TK8-TW3 of geometry and thermodynamics similar to those of TK9-TW3. It seems that the Menter SST model better predicts the level of eddy viscosity in flow, and the rate of dissipation of flow non-uniformities.

The computed efficiency characteristics of the stage as a function of load $u/c_{0T}$ obtained with two different closures of RANS equations – the Baldwin-Lomax and Menter SST turbulence models – are presented in Figure 6 against the experimental graph. For the three examined operating conditions the Baldwin-Lomax model overestimates the stage efficiency, while the Menter SST model apparently underestimates it, but still leaving

room for better accuracy (and higher efficiency) on more refined grids. The differences in estimation of the stage efficiency between the two models are below 1%. Figure 7 shows computed (using both the Baldwin-Lomax and Menter SST turbulence models) and experimental graphs for the stage reaction at the tip and root as a function of load $u/c_{0T}$. Both models yield similar reactions, however they differ from the experimental values by 4% on average. This discrepancy most likely follows from the presence of leakage flows not represented in the computations.

## 4.  HP stage of a real large power steam turbine

In this chapter, we will concentrate on differences in global characteristics as well as in local flow patterns in turbomachinery flows modelled with the help of the Baldwin-Lomax and Menter SST models. An HP stage of a real large power steam turbine whose regular flow patterns are disturbed by the separation at the rotor root is assumed for the computations. The separation is a result of inadequate local incidence on the rotor blade at the root, and can relatively easy be corrected in the design process by more careful stator/rotor matching for the assumed operational range of thermodynamic parameters. However, the considered example provides a fertile field for investigations of the effect of turbulence modelling on computational flow patterns and characteristics, as in the case of adverse pressure gradient flows, including separated flows, the performance of the Baldwin-Lomax model is usually poor and it is expected that the Menter SST model should produce more adequate results.

The tested HP stage of a large power 200 MW steam turbine is a typical impulse stage with short-height blading and aft-loaded stator profiles, and operates at the pressure drop from 79 to 71 bar, inlet temperature – 760 K, flow rate – 165 kg/s, average reaction – 0.20. The aspect ratios are: span/chord – 0.81 (stator) and 2.14 (rotor), pitch/chord – 0.73 (stator) and 0.75 (rotor) , span/diameter – 0.069 (stator) and 0.073 (rotor). The specific heat ratio and gas constant were assumed as $\gamma = 1.29$ and $R = 428$ J/(kgK). The calculations were performed on an H-type grid of 960 000 cells (stator + rotor).

Figure 8 shows the comparison of total pressure contours downstream of the stator trailing edge obtained with Baldwin-Lomax and Menter SST turbulence modelling. The figures apparently do not differ, but the wake is slightly thicker and the total pressure peaks due to secondary flows, especially that at the tip, are closer to the endwalls in the case of the Menter SST model. Velocity vectors at the suction surface of the rotor presented in Figure 9 indicate an earlier onset, in terms of the stream-wise coordinate, and a larger span-wise extension of the secondary flow zones in the Baldwin-Lomax model. A separation from the suction surface at the root also comes into play here. This phenomenon is also clear from Figures 10 and 11 showing velocity vectors and entropy function contours in the rotor 6% of the blade span from the root. The difference in flow patterns between the two models is exceptionally clear. The separation in the Menter SST model is conspicuously delayed and the pitch-wise extension of the separation zone reduced, compared to the predictions of the Baldwin-Lomax model. Entropy function contours in the rotor at subsequent sections, presented in Figure 12 as an illustration of the development of secondary flow patterns and separation throughout the rotor, confirm the tendency already observed in the stator that the loss centres due to secondary flows (at the root due to secondary flows and separation
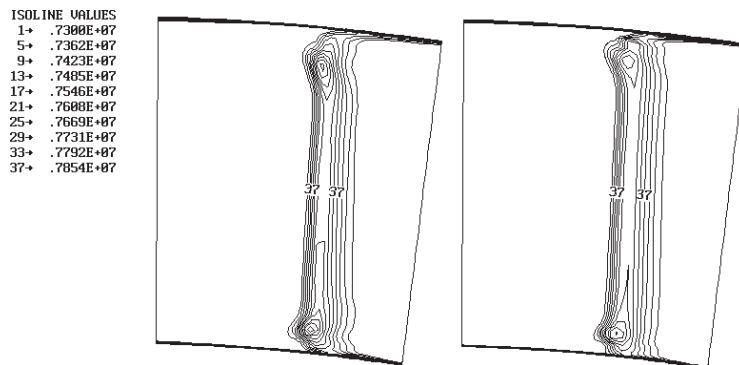
```
ISOLINE VALUES
1→  .7300E+07
5→  .7362E+07
9→  .7423E+07
13→ .7485E+07
17→ .7546E+07
21→ .7608E+07
25→ .7669E+07
29→ .7731E+07
33→ .7792E+07
37→ .7854E+07
```

**Figure 8.** Total pressure contours downstream of the stator: Baldwin-Lomax (left), Menter SST (right)
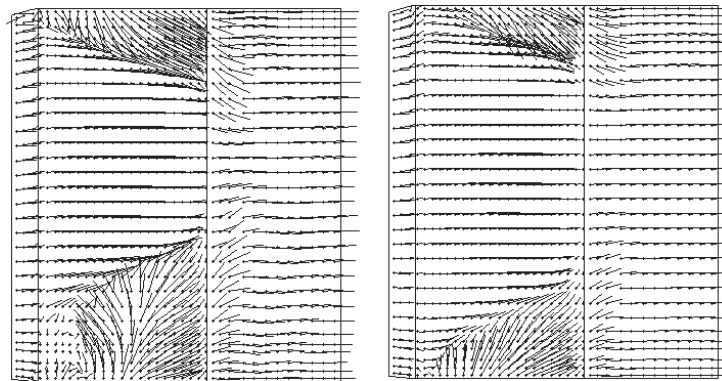


**Figure 9.** Velocity vectors at the suction surface of the rotor: Baldwin-Lomax (left), Menter SST (right)
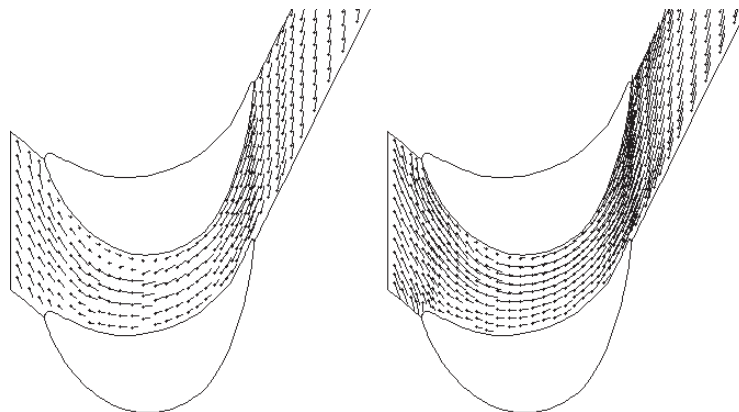


**Figure 10.** Velocity vectors in the rotor 6% blade span from the root: Baldwin-Lomax (left), Menter SST (right)

combined) remain closer to the endwalls, and the wake and boundary layers are slightly thicker in the Menter SST model.
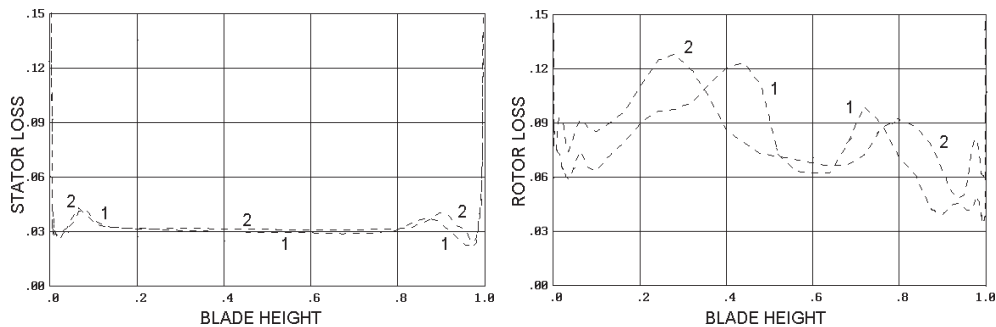
Figure 13 shows a span-wise distribution of kinetic energy losses in the stator and rotor. The definitions of the kinetic energy losses can be found in Nomenclature. The stator loss is captured in the axial gap 10% of the stator axial chord downstream of the trailing
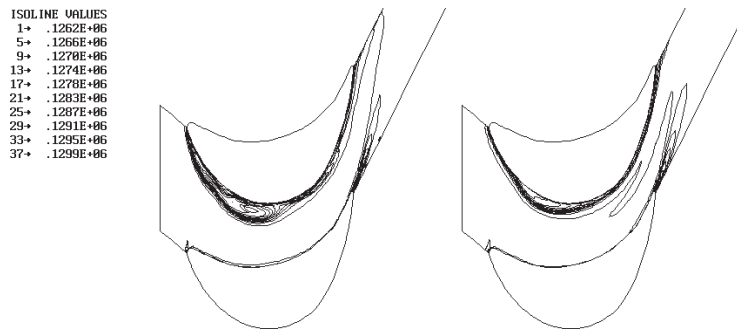
**Figure 11.** Entropy function contours in the rotor 6% blade span from the root: Baldwin-Lomax (left),
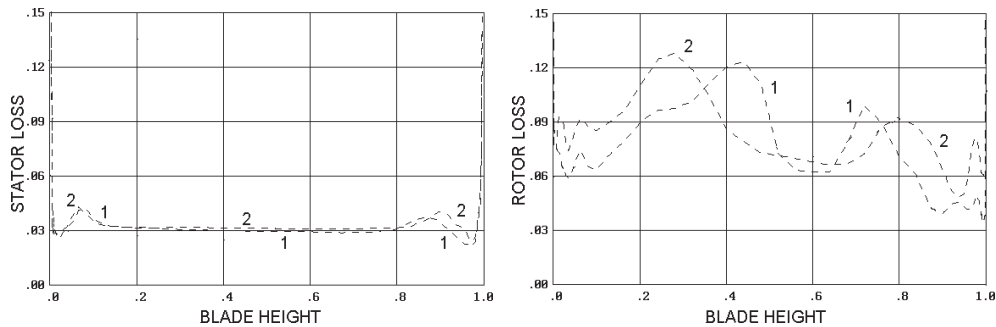Menter SST (right)
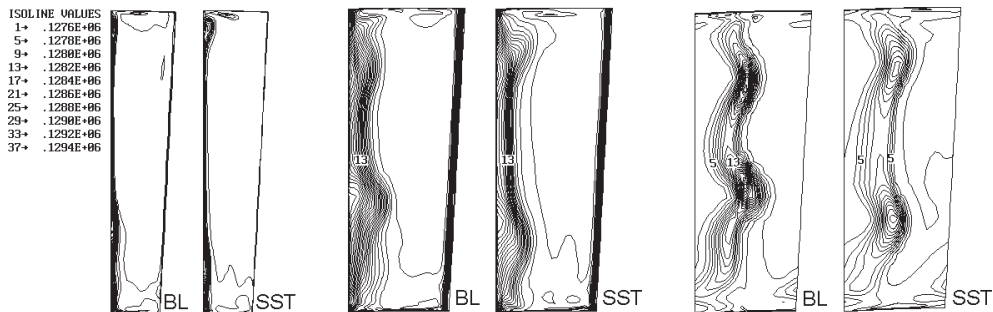


**Figure 12.** Entropy function contours in the rotor: 75% axial chord downstream of the leading
edge (left), at the trailing edge (centre) and 18% axial chord downstream of the trailing edge (right):
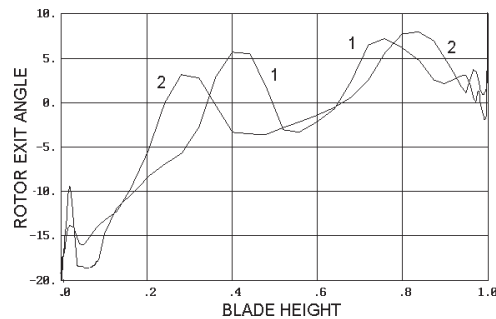Baldwin-Lomax (BL), Menter SST (SST)



**Figure 13.** Span-wise distribution of kinetic energy losses in the stator (left) and rotor (right):
Baldwin-Lomax (1), Menter SST (2)

edge, the rotor loss – 45% of the rotor axial chord downstream of the trailing edge. The
tendency is that there is practically little difference in determination of the profile boundary
layer losses between the two models. The Menter SST model predicts more eddy viscosity
downstream of the trailing edge, which slightly moves up the 2D loss base in the Menter
SST model, compared to that of the Baldwin-Lomax model. The Menter SST model also
predicts more eddy viscosity in the regions of secondary flows, and separation zones,
resulting in more secondary loss and separation loss, say, per volume of the secondary flow
and separation zones. However, the difference in secondary and separation losses between

**Figure 14.** Span-wise distribution of kinetic energy losses in the stage without the exit energy (left) and with the exit energy (right): Baldwin-Lomax (1), Menter SST (2)



**Figure 15.** Span-wise distribution of the rotor exit swirl angle: Baldwin-Lomax (1), Menter SST (2)

the two models is decreased due to a smaller extension of the secondary flow and separation zones in the Menter SST model. The secondary and separation loss maxima are relocated, compared to those of the Baldwin-Lomax model. The pitch/span averaged value of the stator loss differs by 0.2% (Baldwin-Lomax – 3.1%, Menter SST – 3.3%), the rotor loss by 0.6% (Baldwin-Lomax – 7.8%, Menter SST – 8.4%).

From the comparison of span-wise distributions of stage losses without and with the exit energy shown in Figure 14, it is clear again that the Menter SST curves have the 2D loss base slightly moved up and 3D peaks increased and relocated, compared to those of the Baldwin-Lomax model. The relocation of peaks is conspicuous for this stage. However, the pitch/span averaged value of the stage loss without the exit energy differs by 0.3% only (Baldwin-Lomax – 5.1%, Menter SST – 5.4%). For the stage loss with the exit energy the difference is 0.2% (Baldwin-Lomax – 8.0%, Menter SST – 8.2%). The difference in determination of the stage losses with and without the exit energy follows from different evaluation of the exit energy in the two models. First, there is a slight difference in the mass flow rate for the same pressure drop across the stage, the Menter SST model giving 165 kg/s, Baldwin-Lomax – 165.5 kg/s, and as seen from Figure 15, there is also a difference in determination of the mean exit swirl angle: $-11.3°$ for the Baldwin-Lomax model and $-7.6°$ for the Menter SST. The 3D peaks of the exit swirl angle undergo considerable changes in position and magnitude.

In summary, although the flow in the considered stage has a relatively complex nature, mainly due to the interaction of the separation with the main flow and secondary flows,

and there are significant redistributions of losses span-wise between the two models, the difference in pitch/span averaged values of the stage loss is a mere 0.2–0.3%.

## 5. Conclusions

A model air turbine stage and a HP stage of a real large power turbine have been studied using a 3D RANS solver FlowER with closures in the form of: (a) the modified algebraic eddy-viscosity model of Baldwin-Lomax; and (b) the two-equation eddy-viscosity shear stress transport model of Menter, a relatively new two-equation model combining good features of the $k$-$\omega$ and $k$-$\varepsilon$ models. The computations of the model air turbine stage show that the Menter SST model gives better agreement with the experimental data as far as the span-wise distribution of exit velocities and swirl angle. For the considered HP turbine stage, the Menter SST model predicts more eddy viscosity in the wake downstream of the trailing edges, in the regions of secondary flows, and in separation zones. However, a smaller extension of the secondary flow and separation zones is observed in the Menter SST model. There are alterations in span-wise distributions of kinetic energy losses in each blade row and the stage as a whole, by moving slightly up the 2D loss base (increased trailing edge loss), and by increasing and relocating secondary flow (and root separation) peaks, which remain closer to the endwalls in the Menter SST model. There are also changes in the mean values and span-wise distribution of the exit velocity and swirl angle between the two models. However, the differences in pitch/span-averaged values of the overall stage loss do not exceed 1% for the model turbine and 0.3% for the examined HP stage.

## *References*

[1] Baldwin B S and Lomax H 1978 *AIAA Paper* No 78-257
[2] Jones W P and Launder B E 1973 *Int. J. Heat and Mass Transfer* **16** (10) 1119
[3] Launder B E and Sharma B I 1974 *Letters in Heat and Mass Transfer* **1** (2) 131
[4] Chien K Y 1982 *AIAA J.* **20** (1) 33
[5] Wilcox D C 1988 *AIAA J.* **26** (11) 1299
[6] Chima R V 1996 *AIAA Paper* No 96-0248
[7] Wilcox D C 1994 *AIAA J.* **32** (2) 247
[8] Menter F R 1994 *AIAA J.* **32** (8) 1598
[9] Johnson D A and King L S 1985 *AIAA J.* **19** (11) 1684
[10] Yershov S and Rusanov A 1996 *The high resolution method of Godunov's type for 3D viscous flow calculations* Proc. 3 Colloq. Proc. Simulation, Espoo, Finland, June 13–16
[11] Yershov S and Rusanov A 1996 *The application package FlowER for calculation of 3D viscous flows through multi-stage turbomachinery* Certificate of Ukrainian state agency of copyright and related rights, Kiev, Ukraine, February 19
[12] Yershov S, Rusanov A, Gardzilewicz A, Lampart P and Świrydczuk J 1998 *TASK Quarterly* **2** (2) 319
[13] Wilcox D C 1993 *Turbulence modelling for CFD* DCW Industries Inc., La Canada, California
[14] Menter F R 1996 *Trans. ASME J. Fluids Engineering* **118** (3) 514
[15] Larsson J 1996 *Numerical simulation of turbine blade heat transfer* Licentiate of Engineering Thesis, Chalmers University of Technology, Sweden
[16] Yershov S, Rusanov A and Shapochka A 2001 *Proc. Conf. V ISAIF'2001* September 4–7, Gdansk, Poland (to appear)
[17] Yershov S and Rusanov A 1997 *Modification of algebraic turbulence model used in code FlowER* in *Modelling Turbulence in Technical Applications* Copybooks of Institute of Fluid-Flow Machinery, No 486, Gdansk, Poland
[18] Wiechowski S 1988 *Results of investigations of annular cascades TK8, TK9 and models TK8-TW3, TK9-TW3* Rep. Institute of Thermal Engng. Łódź (in Polish)